

Fully Aqueous-Processed Li-Ion Electrodes with Ultra-High Loading and Potential for Roll-to-Roll Processing

Felix Nagler,^[a] Andreas Gronbach,^[a] Andreas Flegler,^[a] and Guinevere A. Giffin^{*[a, b]}

In this study, high- and ultra-high-loading NMC622-based cathodes (7.0 and 18.0 mAh/cm²) and graphite-based anodes (9.0 and 22.5 mAh/cm²) were prepared by using a porous carbon structure as current collector. All electrodes in this work were prepared by an NMP-free, PFAS-free and scalable process. Full cells with areal capacities of 7 mAh/cm² and 18 mAh/cm² were assembled and tested. The results show an excellent cycling stability, reaching up to 950 cycles at 10 mA/cm² for the cells with ultra-high-loading electrodes (capacity 18 mAh/cm²) and 650 cycles at 8 mA/cm² for the cells with high-loading

electrodes (capacity of 7 mAh/cm²). The influence of cathode porosity on the electrochemical performance in cells capacity of 7 mAh/cm² showed that a lower porosity leads to a poorer rate capability as well as a worse cycling capability (400 cycles at 6 mA/cm²). Post-mortem analysis reveal that the anode aging is more pronounced during full cell cycling. Further the scalability of the production process was demonstrated by using a padder tool. With that, cathodes with a loading of 5 mAh/cm² were produced in a roll-to-roll process.

Introduction

Lithium-ion batteries (LIBs) have revolutionized portable electronics and electric vehicles due to their high energy density and long cycle life.^[1,2] The design and characteristics of the electrodes significantly impact the overall energy density of the battery. To further increase the energy density, there has been growing interest in developing anodes and cathodes with high areal loading.^[3–13] This can increase the energy density without changing the cell chemistry by reducing the mass of the inactive cell components (e.g., current collectors and separator) relative to the mass of the active materials. This leads to a more efficient use of materials, which also can help lower the overall cell cost of lithium-ion batteries.^[14] Despite the potential benefits, developing electrodes with high areal loading also presents several challenges. One of the primary challenges is the preservation of the structural integrity during production and cycling. In conventional electrode design, where an electrode composite is coated on a metal foil, cracking and delamination can occur since the mechanical stress within the electrode composite increases with thickness.^[4,15–20] This leads to poor cycling stability. Additionally, the diffusion pathways for the lithium ions through the electrode thickness are longer,

leading to poor rate performance. Efforts to address these limitations have involved the use of two-dimensional meshes and foams^[11,21–24] as well as three-dimensional porous structures^[25–31] as electrode current collectors. These materials have a larger surface area, which should improve the adhesion between the electrode composite and current collector, leading to better mechanical stability.^[16,32] The improved adhesion was observed in a prior study by the authors.^[33] In that work, cathodes with similar loadings (~8 mAh/cm²) were fabricated with both metal foil and porous carbon as current collectors. Upon cycling, the metal-foil-based cathodes exhibited significant capacity fading and partial delamination of the cathode composite from the current collector. In contrast, the cells with the porous carbon current collector showed stable cycling without any indication of a loss of adhesion between the cathode composite and the current collector. Furthermore, the continuous network of the current collector helps to reduce electronic resistance within the electrode, thereby improving the rate performance.^[16,22,29,34]

This study presents the preparation of high-loading (7 and 9 mAh/cm²) and ultra-high-loading (18 and 22.5 mAh/cm²) NMC622 cathodes and graphite anodes with a porous carbon (PC) structure as the current collector. Furthermore, high-loading cathodes (7 mAh/cm²) were prepared with two different porosities (50% and 75%). Full cells with these anodes and based cathodes were assembled (see Table 2) to evaluate electrochemical performance in terms of a current density test and a cycling test to assess long-term stability. To demonstrate the scalability of the electrode manufacturing process, 5 mAh/cm² cathodes were produced using a padder tool, which enabled roll-to-roll (R2R) electrode production. These cathodes were tested in half-cells with lithium metal counter electrodes.

In line *Sustainable by Design* principles, all electrodes were prepared using an aqueous-based process. This eliminates the need for reproductive toxic N-methyl-2-pyrrolidone (NMP)^[30–32] and replaces polyvinylidene fluoride (PVdF) with carboxymethyl

[a] F. Nagler, A. Gronbach, A. Flegler, G. A. Giffin
Fraunhofer R&D Center Electromobility, Fraunhofer Institute for Silicate Research, Neunerplatz 2, 97082 Würzburg, Germany
E-mail: guinevere.giffin@isc.fraunhofer.de

[b] G. A. Giffin
Chair of Chemical Technology of Materials Synthesis, Julius-Maximilians-University Würzburg, Röntgenring 11, 97070 Würzburg, Germany
Supporting information for this article is available on the WWW under <https://doi.org/10.1002/batt.202400732>

© 2024 The Author(s). *Batteries & Supercaps* published by Wiley-VCH GmbH. This is an open access article under the terms of the Creative Commons Attribution License, which permits use, distribution and reproduction in any medium, provided the original work is properly cited.

cellulose (CMC). The use of CMC aligns with current regulatory efforts toward limiting PFAS substances^[35]. Switching to aqueous processing can reduce the cost of cathode production by 50%. This reduction is achieved through lower material expenses and a lower electrode processing cost associated drying and solvent recovery, as demonstrated by Wood et al.^[36] Additionally, aqueous processing offers a significant reduction in capital expenses (CAPEX), as it eliminates the need for the significant safety infrastructure (explosion protection) and solvent recovery systems associated with the use of NMP.^[36] Moreover, aqueous-processed cathodes may be more easily recycled, as the binder can be dissolved in water.^[37,38]

To provide some context for this study, a summary of other studies which have examined the properties and performance of high-loaded electrodes in full-cell configurations, albeit typically with lower current densities, is given here. These studies have been summarized in Table 1 and qualitatively evaluated with respect to long-term cyclability, implementation of NMP-free production with PFAS-free materials, and scalable electrode production methods. Li et al.^[3] used Nb₂O₅ and LFP as the anode and cathode active materials, which were embedded as an electrode composite in a carbon fiber/carbon nanotube matrix. They fabricated a full cell with a capacity of 6.3 mAh/cm² and demonstrated a capacity of 2.3 mAh/cm² at a current density of 2 mA/cm² for 500 cycles. However, during electrode preparation a vacuum filtration step and an 800 °C heat treatment step in N₂ is used, both of which are difficult to scale. Han et al.^[5] demonstrated the manufacturing of NMC811 cathodes with an aluminum mesh structure and graphite anodes in a conductive fiber matrix. Using these components,

they assembled full cells achieving a capacity of approximately 5.0 mAh/cm². The cells demonstrated a good cycling stability, maintaining 80% state of health (SOH) after approximately 700 cycles at a current density of 2.5 mA/cm². The electrodes were fabricated using PVDF as the binder. The manufacturing process appears to be suitable for upscaling, although this was not the focus of the study. Park et al.^[4] demonstrated cycling of full cells with high-loading silicon-based anodes and NMC811-based cathodes. Cycling experiments showed initial capacities of 28.8 mAh/cm² and stable cycling of 50 cycles at 2.0 mA/cm². However, the anode manufacturing includes a heat treatment of 700 °C for 2 h in an argon atmosphere to remove a surfactant, which would hinder scalability of the production process. Furthermore, long-term cycling data at higher current densities was not provided. Gallagher et al.^[4] showed the cyclability of a PVDF-based NMC622 cathode (NMP-processed) with graphite anode with an initial capacity of 5.7 mAh/cm² at 2.2 mA/cm² for 300 cycles. Neidhart et al.^[6] demonstrated the successful R2R processability of aqueous-processed and PFAS-free NMC811 cathodes on aluminum foil with an initial capacity of 7.5 mAh/cm² at 1.7 mA/cm². Full cells with graphite anodes could be stably cycled for 100 cycles. A more extended cycling at higher current densities is not presented. Kwon et al.^[10] report cycling of dry-processed LFP cathodes with a polytetrafluoroethylene (PTFE) binder and graphite anodes. The initial capacity was at 7.8 mAh/cm² at 2.4 mA/cm². The typical end-of-life criterium of 80% SOH was reached after about only 40 cycles. Abe et al.^[9] demonstrated cells with the most impressive cycling stability of high-loading electrodes. The LFP cathode was prepared with an aluminum foam current collector and

Table 1. Properties and cycling performance data of high-loading electrodes reported in the literature.

Current collector	Active materials	Loading in mAh/cm ²	Current in mA/cm ²	Initial Capacity in mAh/cm ²	Cycles (total or until SOH80)	Scalable ^[a]	NMP-free/ PFAS-free	Reference
Carbon fiber/ Carbon Nano-tubes	LFP/Nb ₂ O ₅	6.3	2.0	2.3	500	No, vacuum filtration and 30 min @ 800 °C in N ₂	Yes/Yes	[3]
Al mesh	NMC811/ graphite	5.0	2.5	4.64	~700	Yes, but not demonstrated	Yes/No	[5]
Metal foil	NMC811/ Si	30.9	~2	28.8	50	No, heat treatment of 2 h @ 700 °C in Ar	Yes/Yes	[4]
Metal foil	NMC622/ Graphite	6.6	2.2	5.7	300	Yes	No/No	[6]
Metal foil	NMC811/ Graphite	8.5	1.7	7.5	100	Yes	Yes/Yes	[8]
Metal foil	LFP/Graphite	7.8	2.4	7.8	~40	Yes, but not shown	Yes/No	[10]
Al foam	LFP/Graphite	8.4	1.7	6.3	2000	No, vacuum infiltration	Yes/Yes	[11]
Porous Carbon	NMC622/ Graphite	7.4	8.0	5.0	650	Yes	Yes/Yes	This work
		18.0	10.0	7.6	950			

[a] The scalability is assessed based on existing continuous production processes. Yes: the scalability was demonstrated within the report. Yes, but not shown: the process is in principle scalable, but not shown within the work. The critical step is given in the case of a process that is assessed to be not scalable.

was paired with a graphite anode with an initial capacity of 6.3 mAh/cm^2 at 1.7 mA/cm^2 . The resulting cells were cycled for 2000 cycles. The cathode infiltration was achieved via vacuum infiltration, which may be very challenging to scale up to an industry-relevant process speed.

Results and Discussion

As seen in a previous study of the group,^[33] the full potential of high-loading electrodes ($\geq 7 \text{ mAh/cm}^2$) using a porous carbon structure as current collector, cannot be explored in half-cell tests against a lithium metal counter electrode in liquid carbonate-based electrolytes. In this cell configuration, the lithium metal electrode limits the maximum current density that can be applied and dominates the aging even while cycling at comparably low current densities of 2.0 mA/cm^2 . To test the performance of high-loading electrodes at higher current densities and during long-term cycling, they have to be tested against a suitable counter electrode. To address this challenge, NMC622-based cathodes and graphite-based anodes were produced, both using a porous carbon structure as current collector. As the PC structures consist of carbon fibers, they can contribute to lithium storage when used on anode side. Therefore, the empty PC structures were tested to assess their electrochemical activity in half cells versus a lithium metal counter electrode in the voltage range of $0.01\text{--}1.50 \text{ V}$. As seen in Figure 1a), both tested PC structures (ECM80 and GFD 2.5 EA) show a significant charge capacity (delithiation of PC structure) of around 250 mAh/g for the ECM80 and around 130 mAh/g for the GFD 2.5 EA at a current density of 2.0 mA/cm^2 . Since the voltage profiles (see Figure 1b)) are similar to those of soft carbons,^[39] it can be assumed that the lithium ions can be reversibly inserted into and extracted from the carbon fibers of the PC structures. The microstructure of both empty PC structures is shown in the supplementary in Figure S1. On the cathode side, the electrochemical activity of the empty PC structure was already tested in a previous study of the group.^[33] No electrochemical activity was observed.

To calculate the capacity of the anodes, any capacity associated with the PC structure itself needs to be included. In contrast, in the voltage range used for the cathodes, the capacity of the PC structure can be neglected. In Table 2, the loadings and porosities of the different cathodes and anodes

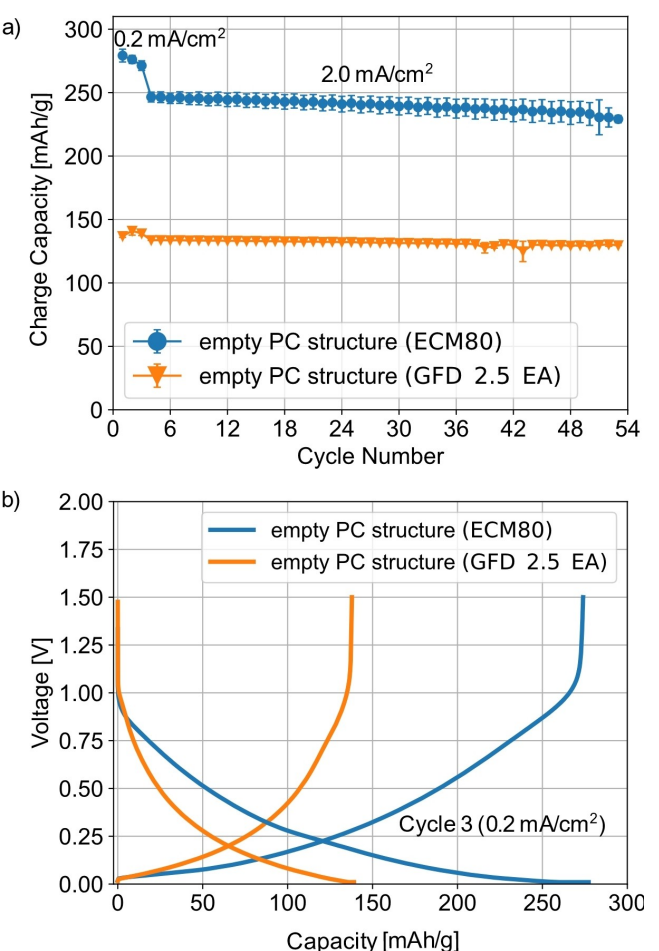


Figure 1. a) Charge capacity (delithiation) and b) voltage profiles of empty PC structures ECM80 and GFD 2.5 EA in half cells in liquid electrolyte. The cells were cycled between $0.01\text{--}1.50 \text{ V}$ at 25°C . The plotted capacities are the mean capacity of two cells.

prepared are summarized, including the capacity of the PC structure on the anode side. Apart from the $\text{PC}_{\text{medium-R2R}}$, all electrodes were prepared via a drop casting procedure at lab scale. The $\text{PC}_{\text{medium-R2R}}$ were produced in a roll-to-roll process using a padder tool. For the full cells, the loadings of the cathodes and anodes were adjusted to get a N/P ratio of around 1.25. To obtain a similar anode porosity of around 90%, the ECM80 was used as current collector structure for the PC_{high}

Table 2. Cathode and anodes properties of the different cells PC_{high} (55 %), PC_{high} (75 %), $\text{PC}_{\text{ultra-high}}$, $\text{PC}_{\text{medium-lab}}$ and $\text{PC}_{\text{medium-R2R}}$. The latter two cathodes were only tested in half cells against a lithium-metal counter electrode.

Cell name	Cathode current collector	Cathode thickness/porosity	Cathode loading in mAh/cm^2	Anode current collector	Anode thickness/porosity	Anode loading in mAh/cm^2	N/P
PC_{high} (55 %)	ECM80	$320 \mu\text{m}$ [a]/55 %	7.0	ECM80	$1000 \mu\text{m}$ /85 %	8.6	1.23
PC_{high} (75 %)	ECM80	$1000 \mu\text{m}$ /75 %	7.4	ECM80	$1000 \mu\text{m}$ /85 %	9.2	1.24
$\text{PC}_{\text{ultra-high}}$	ECM80	$1000 \mu\text{m}$ /55 %	18.0	GFD 2.5 EA	$2500 \mu\text{m}$ /82 %	22.5	1.25
$\text{PC}_{\text{medium-lab}}$	ECM80	$1000 \mu\text{m}$ /85 %	4.6	–	–	–	–
$\text{PC}_{\text{medium-R2R}}$	ECM80	$1000 \mu\text{m}$ /85 %	5.0	–	–	–	–

[a] The PC_{high} (55 %) was the only sample which was calandered after infiltrating. By that the original thickness of around $1000 \mu\text{m}$ was reduced to $320 \mu\text{m}$.

anodes and the GFD 2.5 EA for the PC_{ultra-high} anodes. If the ECM80 had been used to produce PC_{ultra-high} anodes with similar loading, the anodes would have had porosities of around 60%. To get an idea of the influence of the cathode porosity on the electrochemical performance, two different cathode porosities with similar loading were tested (PC_{high} with porosities of 55% and 75%). The PC_{medium-lab} and PC_{medium-R2R} were only tested in half cells against a lithium-metal counter electrode.

For the electrochemical testing of the full cells, a current density test was used instead of a traditional C-rate. In a C-rate test, cells with different capacities would be tested with very different currents at the same C-rate. With a current density test, the same current is applied to all cells independent of the cell capacity. Although arguments can be made for and against either method, it is the opinion of the authors current density test allows a better comparability of the data, particular in terms of the polarization phenomena occurring in the cells. When the resulting discharge capacity is normalized by the nominal capacity, the result is essentially a capacity retention value. This value indicates the percentage of the cells' capacity that can be extracted at different current densities.

In the current density test (Figure 2), all full cells show discharge capacities (DC) close to their nominal capacity at low current densities ($\leq 2.0 \text{ mA/cm}^2$). At 2.0 mA/cm^2 the PC_{ultra-high} cells have a DC of 15.8 mAh/cm^2 (equal to $155 \text{ mAh/g}_{\text{CAM}}$, CAM=cathode active material), which is around 88% of the nominal capacity of 18.0 mAh/cm^2 (which would equal $175 \text{ mAh/g}_{\text{CAM}}$). The PC_{high} (75%) and PC_{high} (55%) cells show a DC of 5.9 and 5.8 mAh/cm^2 , respectively, at 2.0 mA/cm^2 . This is equal to 80% and 82% of the nominal capacity, respectively. The tendency for the PC_{ultra-high} cells to have a higher DC in relation to the nominal capacity than both of the PC_{high} cells can be explained by the fact that the electrochemically active surface area increases with higher loading. Since the current density is set in relation to the electrode area and not the surface area of the NCM622 particles, higher loadings lead to lower polarization in the cells, because the same current is applied to a larger active material surface area. At higher current densities, the DCs of the PC_{ultra-high} decline. Here, diffusion polarization most likely leads to higher cell polarization and hence lower DC. Due to the high electrode thicknesses (cathode $\sim 1000 \mu\text{m}$ and anode $\sim 2500 \mu\text{m}$), the lithium-ion diffusion pathways are quite long. Thus, diffusion is expected to limit performance especially at higher current densities. The increased polarization at higher current densities are clearly visible in the voltage profiles in Figure S2. At a current density of 18 mA/cm^2 , which is equal to 1 C for the PC_{ultra-high}, the DC of these cells is 3.8 mAh/cm^2 , which is equal to 21% of the nominal capacity. A decline in the DCs at higher current densities is less evident for both PC_{high} (75%) and PC_{high} (55%). Furthermore, PC_{high} (75%) has higher DCs than the PC_{high} (55%) at higher current densities ($\geq 6 \text{ mA/cm}^2$). For example, at a current density of 8.0 mA/cm^2 , which is slightly higher than 1 C for both cells, PC_{high} (75%) has a DC of 4.9 mAh/cm^2 and the PC_{high} (55%) of 3.8 mAh/cm^2 , which is equal to 66% and 54% of the nominal capacity, respectively. The reason for the better performance of the PC_{high} (75%) compared to the PC_{high} (55%) is

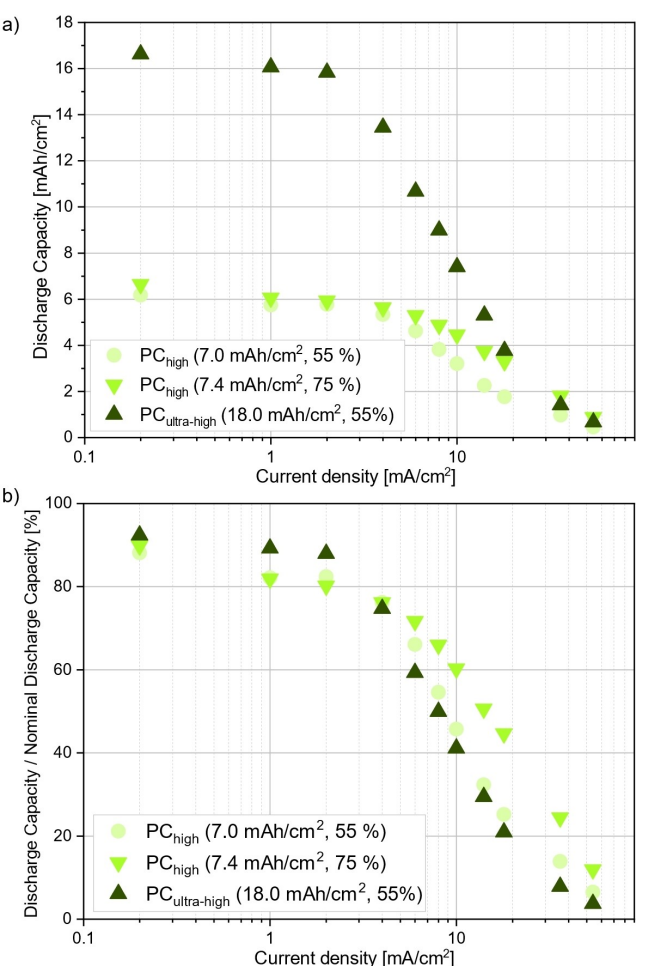


Figure 2. Current density test of PC_{high} (55%), PC_{high} (75%) and PC_{ultra-high} between 0.2 and 54 mA/cm². a) Discharge capacities in mAh/cm² and b) percentage of nominal discharge capacity. The plotted values are the mean discharge capacity of two cells each and five cycles at each current density.

likely the lower tortuosity of the more porous cathode. Even though the cathode of the PC_{high} (55%) is thinner than the cathode of the PC_{high} (75%) ($320 \mu\text{m}$ compared to $1000 \mu\text{m}$), the diffusion pathway of PC_{high} (75%) might be lower due to the higher cathode porosity. This would explain the lower polarizations seen for the PC_{high} (55%) in Figure S2a). It can be concluded from the current density test results that for all cells almost the full theoretical capacity at this cut-off voltage can be cycled at low current densities ($\leq 2.0 \text{ mA/cm}^2$). At higher current densities, where diffusion polarization has a more significant impact, the DCs decrease for all cells, but a higher cathode porosity leads to a better performance in terms of DC.

To investigate the long-term cyclability, the cells were cycled with a fixed current density until they reach 80% of their initial capacity (state of health 80%, SOH80) (see Figure 3). For PC_{ultra-high}, a current density of 10 mA/cm^2 was chosen, which is equivalent to a C-rate slightly above C/2. PC_{ultra-high} shows an excellent cycling stability. The initial DC is at 7.6 mAh/cm^2 (equal to about $75 \text{ mAh/g}_{\text{CAM}}$) and it is possible to cycle the cells for over 950 cycles at 10 mA/cm^2 before SOH80 (6.1 mAh/cm^2 or $60 \text{ mAh/g}_{\text{CAM}}$) is reached. For the PC_{high} (75%), a current

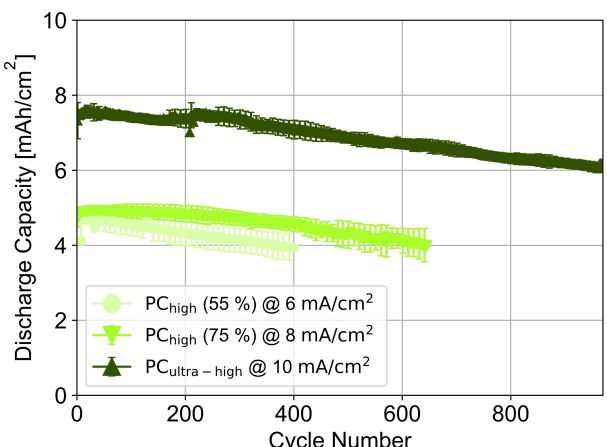


Figure 3. Long-term cycling of PC_{high} (55%), PC_{high} (75%) and PC_{ultra-high}. The current densities for PC_{high} (55%), PC_{high} (75%) and PC_{ultra-high} were chosen to be 6 mA/cm², 8 mA/cm² and 10 mA/cm², respectively. Cycling was stopped at SOH80. The DC values are the mean of that from two cells, with the standard deviation given as error bar.

density of 8 mA/cm² was chosen, which is also equivalent to a C-rate slightly above 1 C. In this case, 650 cycles can be performed before 80% of the initial capacity of 5.0 mAh/cm² is reached (SOH80: 4.0 mAh/cm² or 95 mAh/g_{CAM}).

For better comparison of both PC_{high} types, the current densities of the PC_{high} (55%) was set to 6.0 mA/cm² for cycling to have a similar initial capacity of 5.0 mAh/cm². The PC_{high} (55%) can be cycled for around 400 cycles before SOH80 (4.0 mAh/cm² or 95 mAh/g_{CAM}) is reached. The reason for the reduced cycling stability of the PC_{high} (55%) compared to the PC_{high} (75%) might be explained by increased particle cracking during calendaring. The higher mechanical stress could lead to crack formation, which would increase the active sites for electrolyte side reactions. This would lead to a reduced cycling stability. Similar effects were observed by Stein et al.^[40]

It is worth mentioning that the measurements were performed using a standard electrolyte (1 M LiPF₆ in EC/EMC 3:7 wt%/wt%) without the addition of any electrolyte additives. As known from literature,^[41] additives increase the cyclability due to improvement of the solid electrolyte interphase (SEI) and/or the cathode electrolyte interphase (CEI) properties or the ionic conductivity of the electrolyte. Nonetheless, the cycling performance presented in this work, 7.6 mAh/cm² at 10.0 mA/cm² for 950 cycles and 5.0 mAh/cm² at 8.0 mA/cm² for 650 cycles, is promising in comparison to other literature reports (see Introduction and Table 1), particularly considering that an aqueous process with a nickel-rich cathode

material, PFAS-free binders and scalable production process is used.

To better understand the aging mechanisms, post mortem studies were performed for one of the PC_{high} (75%) cells. To differentiate between aging effects of the anode and the cathode, both electrodes were tested separately in half cells against a lithium metal counter electrode. EIS measurements as well as a rate test were conducted after the initial formation of the lithium metal cells (5 cycles at 0.2 mA/cm²). Pristine anodes and cathodes were also tested as a reference (also after initial formation of 5 cycles at 0.2 mA/cm²). The impedance of both the anode and cathode is higher for the aged electrodes compared to the pristine electrodes (see Figure 4a) and b). Four features can be seen in the Nyquist plots of all measurements except that of the anode_{aged} (PC_{high}, 75%, 650 cycles) (see Figure 4b)). The high-frequency intercept can be assigned to the ohmic resistance R_{IR} of the cells. The semicircle at the highest frequencies is attributed to the resistance between the electrode composite and the current collector R_e.^[42–44]

The semicircle at medium frequencies can be assigned to the solid electrolyte interphase with the corresponding resistance R_{SEI}.^[45–54] The semicircle at low frequencies can be linked to the charge-transfer resistances R_{CT}.^[42–45] For the spectra of the anode_{aged} (PC_{high}, 75%, 650 cycles), the semicircles linked to R_e and R_{SEI} are hard to separate. Hence, only one, instead of two semicircles, is used for fitting in the high frequency region. The fitted values for the different resistances are summarized in Table 3. The total impedance R_{total} of the anode increases significantly from 47.3 Ωcm² to 142.6 Ωcm² during cycling (from anode_{pristine} (PC_{high}, 75%, 5 cycles) to anode_{aged} (PC_{high}, 75%, 650 cycles)). The ohmic resistances R_{IR} stays more or less constant (4.8 to 5.8 Ωcm²). As the features leading to R_e and R_{SEI} are overlapped for the spectra of the anode_{aged} (PC_{high}, 75%, 650 cycles), it is not possible to determine whether both or only one of those resistances is increasing. Nonetheless, the sum of the resistances from these features increases from 35.5 Ωcm² (10.6 + 24.9 Ωcm²) to 85.5 Ωcm². R_{CT} increases from 6.9 Ωcm² to 51.3 Ωcm². The higher resistances originate from the SEI growth on the graphite surface during cycling. Similar impedance growth was observed in other aging studies.^[47]

For the cathodes (see Figure 4a)), an increase in R_{total} from 21.9 to 24.4 Ωcm² can also be observed. However, it is significantly less pronounced than that of the anodes. The most significant increase is determined for the R_{CT} (4.5 Ωcm² – 12.0 Ωcm²). This is caused by the cathode electrolyte interphase, which is formed on the surface of the NMC622 particles during cycling. The decrease of R_{SEI} for the cathode_{aged} (PC_{high}, 75%, 650 cycles) (8.9 – 3.8 Ωcm²) might be caused by the

Table 3. Resistances determined by fitting the EIS data.

	R _{IR} in Ωcm ²	R _e in Ωcm ²	R _{SEI} in Ωcm ²	R _{CT} in Ωcm ²	R _{total} in Ωcm ²
anode _{pristine} (PC _{high} , 75%, 5 cycles)	4.8	10.6	24.9	6.9	47.3
anode _{aged} (PC _{high} , 75%, 650 cycles)	5.8	85.5	–	51.3	142.6
cathode _{pristine} (PC _{high} , 75%, 5 cycles)	4.3	4.2	8.9	4.5	21.9
cathode _{aged} (PC _{high} , 75%, 650 cycles)	4.7	3.9	3.8	12.0	24.4

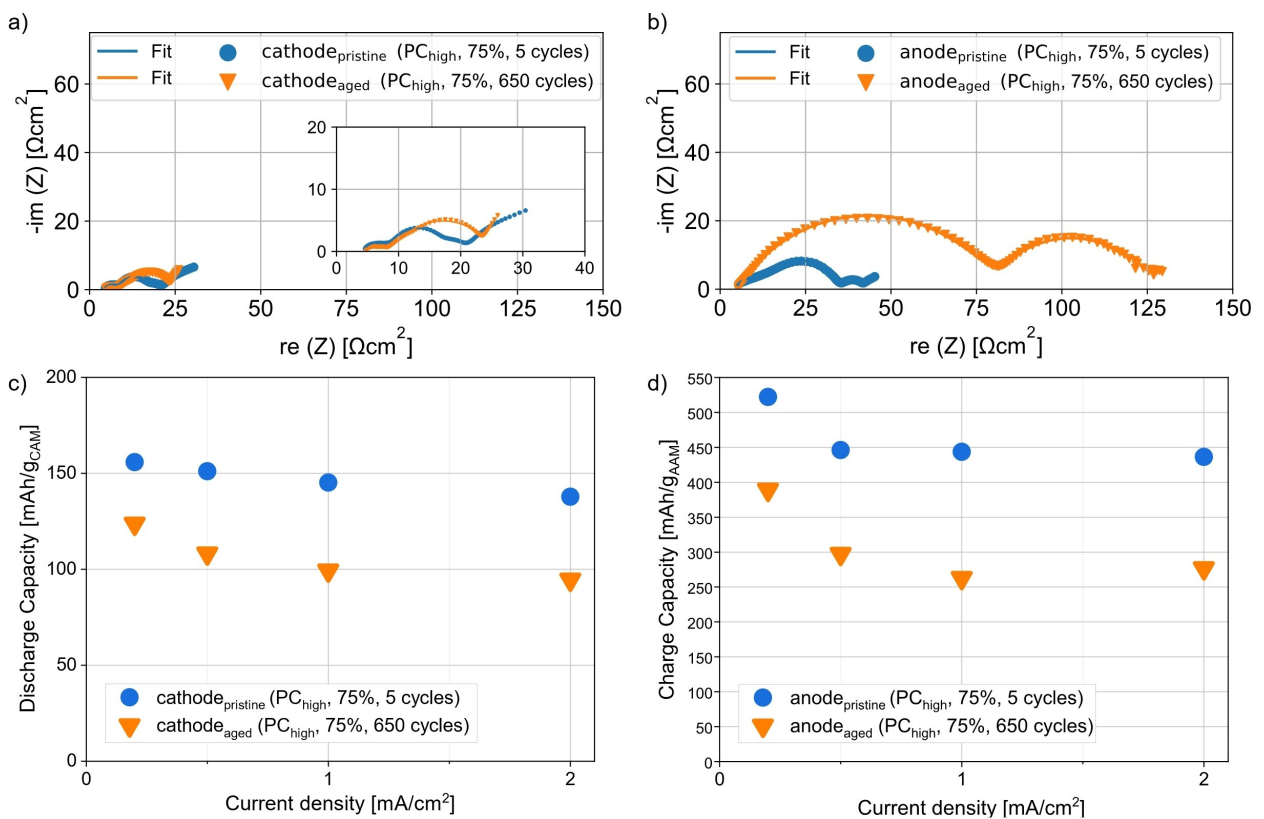


Figure 4. Electrochemical post-mortem characterizations of cathode and anode of PC_{high} (75%) in half cells against a lithium metal counter electrode. For comparison a pristine electrode is tested under the same conditions. a) and b) Nyquist plots of EIS measurements including data fits. c) and d) current density tests.

preparation of the lithium metal counter electrode. To remove the native oxide layer from the lithium surface, the lithium foil was gently scraped with a ceramic knife. It is possible that the resulting surface of the lithium metal electrodes were slightly different due to the manual processing, resulting in different R_{SEI} values. In summary, the total impedance increase of the anode is much more significant than that of the cathode (300% compared to 10%), which indicates a more pronounced the anode degradation.

In the rate test, both the anode_{aged} (PC_{high}, 75%, 650 cycles) (Figure 4d)) and the cathode_{aged} (PC_{high}, 75%, 650 cycles) (Figure 4c)) show lower capacities compared to the pristine electrodes. This difference cannot be explained by loss of lithium inventory as a potential loss of lithium would be compensated by the lithium metal counter electrode in the half cell configuration. Therefore, the loss in capacity of both electrodes can likely be attributed to additional polarizations arising from degradation during cycling. This is in accordance with the EIS measurements. The charge capacity of the anode half cells (delithiation of the graphite anode), which is above the theoretical capacity of graphite (372 mAh/g_{AAM}, AAM = anode active material), can be explained by the additional capacity of the PC structure as seen in Figure 1a). The anode_{pristine} (PC_{high}, 75%, 5 cycles) has a capacity of 522 mAh/g_{AAM} at a current density of 0.2 mA/cm². In comparison, the anode_{aged} (PC_{high}, 75%, 650 cycles) has only a capacity of 389 mAh/g_{AAM}, which is

a decrease of 25 %. The cathode_{pristine} (PC_{high}, 75%, 5 cycles) has a capacity of 155 mAh/g_{CAM} at a current density of 0.2 mA/cm² and the cathode_{aged} (PC_{high}, 75%, 650 cycles) 125 mAh/g_{CAM}. This is equal to a decrease of 20%. The results indicate that although both electrodes degrade during full cell cycling, the anode degradation is more pronounced.

The SEM images in Figures S3 and S4 in the supplementary information reveal no significant differences in the microstructure of the electrodes before and after cycling. The electrode composites remain firmly attached to the carbon fibers of the PC structure of all samples. Both aged electrodes seem to show a slight increase in thickness, but this could be due to electrolyte contact in the cell.

SEM images of the active materials within the electrodes is shown in Figure 5. There are clear differences in the graphite particle surface of the aged anodes (see Figure 5a and b)). The anode_{pristine} (PC_{high}, 75%, no electrolyte contact) exhibits a clean surface. In contrast, the SEI is evident on the surface of the aged anode particles (anode_{aged} (PC_{high}, 75%, 650 cycles)). There is no significant changes in the surface morphology of the cathode particles (see Figure 5c) and d)). Both the pristine cathode (cathode_{pristine} (PC_{high}, 75%, no electrolyte contact)) and the aged cathode (cathode_{aged} (PC_{high}, 75%, 650 cycles)) are partially covered by conductive carbon or binder. In the areas where secondary particles are not covered with conductive carbon or binder, there is a clean and smooth surface

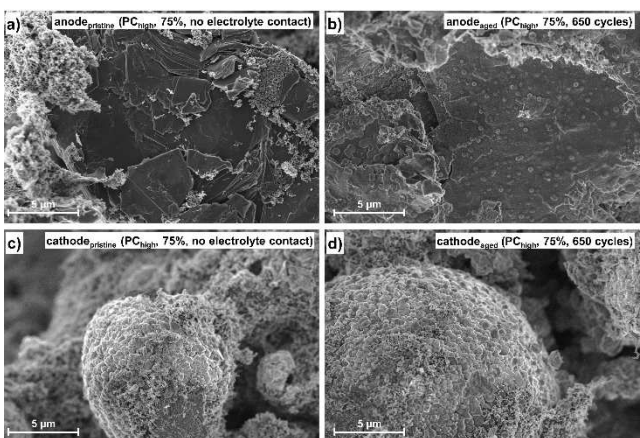


Figure 5. SEM images of a) pristine anode ($\text{anode}_{\text{pristine}}$ (PC_{high} , 75 %, no electrolyte contact))), b) cycled anode ($\text{anode}_{\text{aged}}$ (PC_{high} , 75 %, 650 cycles))), c) pristine cathode ($\text{cathode}_{\text{pristine}}$ (PC_{high} , 75 %, no electrolyte contact))), d) cycled cathode ($\text{cathode}_{\text{aged}}$ (PC_{high} , 75 %, 650 cycles))).

suggesting minimal surface film formation for cathodes during cycling.

The SEM images illustrate that the PC structure is effective in maintaining the structural integrity of high-loading electrodes during long-term cycling on both the anode and cathode side. While the cathode material remains largely unchanged throughout the cycling process, the surface morphology of the graphite on the anode side indicates SEI formation. Consequently, typical aging phenomena, such as impedance increase and loss of lithium inventory resulting from SEI growth, are the primary causes of capacity fading during cycling, rather than electrode degradation mechanisms such as delamination or contact loss of the active materials from the PC structure. This result is consistent with the results obtained from the EIS measurements, which also reflect an increase in impedance consistent with SEI growth.

A padder tool was used to determine if the infiltration of the PC structure is scalable. The process of infiltrating the ECM80 PC structure with the aqueous cathode slurry is schematically shown in Figure 6a). The ECM80 is pulled through a slurry reservoir, where the slurry infiltrates the porous structure. Afterwards, the infiltrated PC structure passes through two rolls, which delivers a defined pressure to homogenize the distribution of the infiltrated slurry and squeeze out excess slurry (see Figure 6c). Cathodes with a similar loading were produced by the lab-scale drop casting method ($\text{PC}_{\text{medium-lab}}$) as a reference. Both cathodes, the $\text{PC}_{\text{medium-lab}}$ and $\text{PC}_{\text{medium-R2R}}$, were tested in half cells against a lithium metal counter electrode. The cycling performance is shown in Figure 7a). The cathodes show a similar initial DC ($\text{PC}_{\text{medium-R2R}}$: 163 mAh/g_{CAM}; $\text{PC}_{\text{medium-lab}}$: 160 mAh/g_{CAM}). After cycling for 50 cycles at a current density of 2.0 mA/cm², the $\text{PC}_{\text{medium-R2R}}$ has a DC of 152 mAh/g_{CAM} and the $\text{PC}_{\text{medium-lab}}$ of 148 mAh/g_{CAM}. This corresponds to a capacity retention of 93% for both cells. The voltage profiles are very similar and only show a small deviation at the end of charge and discharge (see Figure 7b)), explaining the marginal difference in the DCs. These small deviations can be explained by the

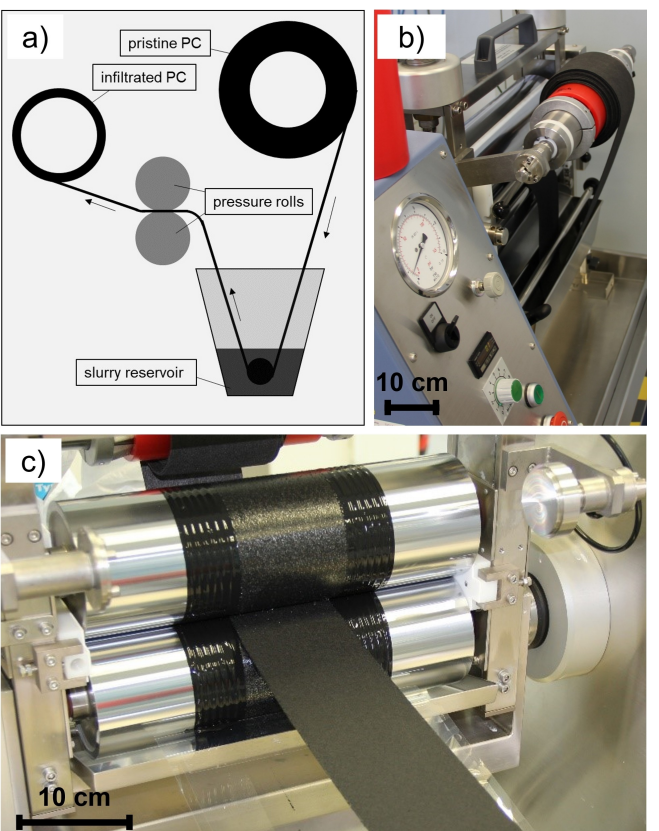


Figure 6. a) schematic process illustration of R2R infiltration process of the PC structures with a padding tool, b) and c) images of padder tool during R2R processing.

slightly different cathode loading ($\text{PC}_{\text{medium-R2R}}$: 5.0 mAh/cm², $\text{PC}_{\text{medium-lab}}$: 4.6 mAh/cm²), and thus the higher active material surface area of $\text{PC}_{\text{medium-R2R}}$. As both cathodes are tested at the same current density, which is set in relation to the electrode area and not the surface area of the NCM622 particles, the polarizations should be slightly lower for the higher loading cathodes, since the same current is applied to a larger active material.

The comparison of the lab-scale and roll-to-roll results implies that the infiltration of the PC structure is scalable to a continuous process without performance losses. It is likely possible to infiltrate larger quantities of PC-based cathodes quickly and easily.

Conclusions

The successful production of cells with high-loading NMC622 cathodes and graphite-based anodes is reported in this study. The electrodes were prepared using an aqueous, PFAS-free and scalable production method. Full cells with capacities of around 7 and 18 mAh/cm² were prepared. The current density test demonstrates that almost the full capacity can be reversibly cycled at low current densities ($\leq 2.0 \text{ mA/cm}^2$). At higher current densities, diffusion polarization leads to lower capacities for all cells. A higher cathode porosity of 75 % (PC_{high} 75 %) leads to a

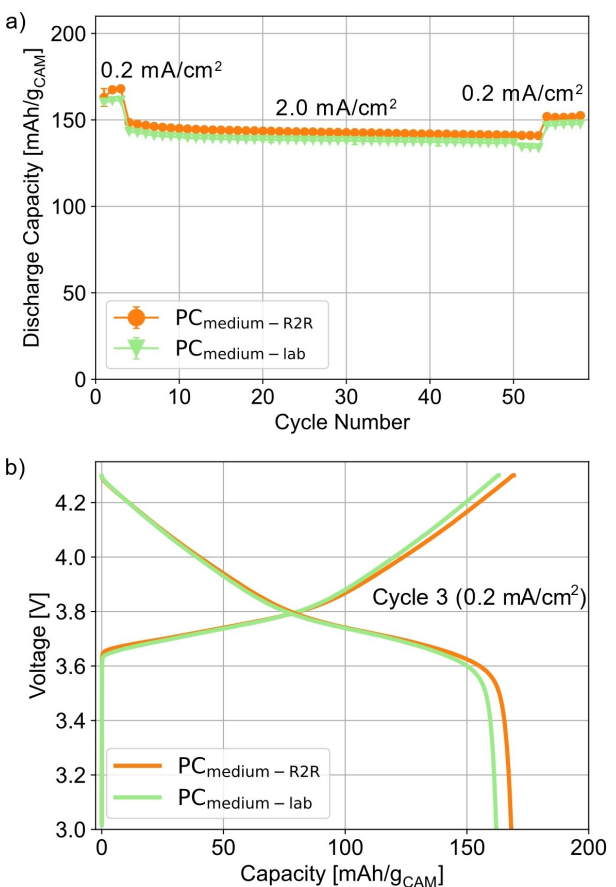


Figure 7. a) Discharge capacities of PC_{medium}-R2R and PC_{medium}-lab measured in half cells with a lithium metal counter electrode. The values are the mean discharge capacity of three cells, with the standard deviation given as error bars. b) Voltage profile of 3rd cycle at 0.2 mA/cm² of a representative cell.

better performance compared to similar loading but lower porosity cathodes (PC_{high}, 55%). All cells demonstrated an excellent long-term cycling stability. The PC_{ultra-high} delivered an initial capacity of around 7.5 mAh/cm² and could be cycled at a current density of 10 mA/cm² before SOH₈₀ is reached after 950 cycles. The PC_{high} (75%) delivered an initial capacity of around 5.0 mAh/cm² at 8 mA/cm² and reached SOH₈₀ after ca. 650 cycles. The SEM images of the cycled electrodes showed no significant change in the microstructure after cycling, suggesting that the structural integrity of the high-loading electrodes is preserved during long-term cycling. The EIS measurements of the cycled electrodes indicate that the aging of the anode is more pronounced than for the cathode. The total impedance increases by 300% for the anode and only by 10% for cathode. The scalability of the production process is demonstrated using a padder tool in a R2R process. The electrochemical performance of the R2R cathode prepared is almost identical to that of cathodes with similar loading prepared at the lab scale. This work demonstrates that the use of PC structure as current collector enables not only electrodes with a high-loading, but also offers an environmentally friendly and scalable process.

Experimental Section

Electrode Processing

Cathode Slurry

An aqueous slurry consisting of 89 wt% NCM622 active material (Lot number: 5557180a, Umicore S.A., Belgium), 4 wt% sodium carboxymethyl cellulose (CMC, MW ~250 000 g/mol, degree of substitution 0.9, Sigma Aldrich Chemie GmbH) as binder, 4 wt% Super C65 (C-NERGY™, Imerys S.A) as conductive carbon and 3 wt% BYK3450 (silicone surfactant, BYK Additives & Instruments) as an infiltration additive (IA) was prepared. The CMC was therefore dissolved in deionized water overnight. The water amount was adjusted with respect to the solid components to 120 wt% for the PC_{high} cathodes and to 80 wt% for the PC_{ultra-high} cathodes. To the CMC-water solution the NCM622 and the Super C65 were added. The resulting slurry was then mixed for 2 h with a SpeedMixer (DAC 400.1 Vac-P, Hauschild GmbH & Co. KG). The IA was added to the slurry for the last ten minutes of the mixing process. The IA is added to ensure a fast and homogeneous infiltration process into the hydrophobic porous carbon structure by reducing the surface tension.

Cathode Infiltration (Lab Scale)

To infiltrate the porous carbon (PC) structure ECM80 (SIGRACET®, SGL Carbon SE) at lab scale, the aqueous slurry was drop-casted on both sides of the ECM80 for 2 min each. Then, the infiltrated ECM80 was pre-dried for 1 h at 80 °C. For the PC_{medium-lab} cathodes, the just infiltrated cathodes were pressed with a plastic roll to squeeze out some of the slurry to obtain a loading comparable to the PC_{medium-R2R} before pre-drying. For the PC_{high} and PC_{ultra-high} this squeezing was not performed. For the PC_{ultra-high}, the drop-casting process was repeated one time after the pre-drying. For the PC_{high} with a porosity of 55%, the dried cathodes were calendered to a thickness of 320 µm. The PC_{high} with a porosity of 75% and the PC_{ultra-high} with a porosity of 55% and PC_{medium-lab} were not calendered. Disc electrodes with a diameter of 16 mm were punched out for all cathodes and dried under vacuum for 12 h at 150 °C. The properties of the cathodes are summarized in Table 2.

Cathode Infiltration (Roll-to-Roll, Padder Tool)

To scale the cathode infiltration, a padder tool (2-roll padder type HVF, Werner Mathis AG) was used to demonstrate the transfer to a continuous roll-to-roll process. The cathode slurry was prepared as described above and contained 120 wt% of water compared to the solid components. The roll velocity of the padder tool was adjusted to 0.1 m/min and a roll pressure of 1 bar was used. The infiltrated cathodes were directly pre-dried for 1 h at 80 °C. Afterwards the PC_{medium-R2R} were not calendered similar to the PC_{medium-lab}. Disc electrodes with a diameter of 16 mm were punched out and dried under vacuum for 12 h at 150 °C.

Anode Slurry

An aqueous graphite slurry was prepared with 92 wt% graphite, 2 wt% CMC, 2 wt% styrene-butadiene rubber (SBR, Targray Technology International Inc.) and 4 wt% of Super C65. The CMC was dissolved in deionized water overnight before adding the graphite and Super C65. The slurry was mixed for 2 h with a SpeedMixer. The SBR was added for the last 10 minutes of mixing. The water amount was adjusted to 325 wt% for anodes to achieve loadings to

match the PC_{high} cathodes and to 290 wt% to match the $\text{PC}_{\text{ultra-high}}$ cathodes.

Anode Infiltration

The slurries were drop-casted in two different porous carbon structures, for 2 min for each side. ECM80 (SIGRACET®, SGL Carbon SE) was used as PC structure to prepare anodes matching the PC_{high} cathodes. A thicker PC structure, GFD 2.5 EA (SIGRACELL®, SGL Carbon SE), which has a thickness of 2500 μm was used to prepare matching anodes for the higher-loading $\text{PC}_{\text{ultra-high}}$ cathodes. The anodes were directly pre-dried for 1 h at 80 °C after infiltration. Disc electrodes with a diameter of 17 mm were punched out and dried under vacuum for 12 h at 110 °C. The properties of the anodes are summarized in Table 2.

Half-Cell Tests Using a Lithium-Metal Counter Electrode

The $\text{PC}_{\text{medium-lab}}$ and $\text{PC}_{\text{medium-R2R}}$ cathodes as well as the empty, uninfiltrated PC structures (ECM80 and GFD 2.5 EA) were tested in half cells with lithium metal (Sigma-Aldrich) as counter electrode, a glass-fiber separator (Whatman GF/C) and 400 μl of 1 mol/L LiPF_6 in EC/DMC 1:1 wt%/wt% (LP30, BASF SE) as electrolyte. The cells contain an excess of electrolyte. The lithium metal was scraped with a ceramic knife to remove the oxide layer before use. The cells were assembled in ECC-Ref cells (EL-Cell GmbH) in an argon-filled glovebox (GS-Glovebox, $\text{O}_2 < 1.0 \text{ ppm}$, $\text{H}_2\text{O} < 0.1 \text{ ppm}$). Cycling tests were performed on an electrochemical workstation (Maccor, Series 4000, Maccor Inc.) at 25 °C (IPP260, Memmert GmbH + Co. KG).

The half cells with $\text{PC}_{\text{medium-lab}}$ and $\text{PC}_{\text{medium-R2R}}$ were charged with a constant-current constant-voltage procedure (CCCV) and discharged with a constant-current procedure (CC) between 3.0 and 4.3 V. The CV-step was terminated at a current of 0.5 mA. For formation, the cells were cycled three times with a current density of 0.2 mA/cm². Subsequently, the cells were cycled at 2.0 mA/cm² for 50 cycles before cycling again at 0.2 mA/cm² for three cycles.

The half cells with the empty PC structures were discharged with CCCV and charged with CC between 0.01–1.50 V. The CV-step was terminated at a current of 0.5 mA. The cells were cycled three times with a current density of 0.2 mA/cm² during the formation cycles, and then at 2.0 mA/cm² for 50 cycles.

Full Cell Tests

The full cells with the PC_{high} (55%), PC_{high} (75%) and $\text{PC}_{\text{ultra-high}}$ electrodes were prepared in ECC-PAT-Core cells (EL-Cell GmbH) with a glass-fiber separator (Whatman GF/C). The anodes and cathodes were chosen according to Table 2 to yield N/P ratios around 1.25. The amount of electrolyte (1 mol/L LiPF_6 in EC/EMC 3:7 wt%/wt% (LP57, BASF SE)) was 450 μl for the PC_{high} and 800 μl for the $\text{PC}_{\text{ultra-high}}$. The electrochemical tests were performed on an electrochemical workstation (Maccor, Series 4000, Maccor Inc.) at 25 °C. For all cells, a formation procedure with two cycles at 0.2 mA/cm² and two cycles at 0.5 mA/cm² in a voltage range of 3.0–4.2 V was performed. A current density test was then performed with current densities of 0.2, 1.0, 2.0, 4.0, 6.0, 8.0, 10.0, 14.0, 18.0, 36.0, 54.0 mA/cm². The cells were cycled between 2.7–4.2 V for 5 cycles at each current density with a CCCV procedure during charge and a CC procedure during discharge. The CV-step was terminated at a current of 0.5 mA. Subsequently, the cells were cycled at a constant current density, 8 mA/cm² for PC_{high} (75%), 6 mA/cm² for PC_{high} (55%) and 10 mA/cm² for $\text{PC}_{\text{ultra-high}}$, in the voltage window of 2.7–4.2 V with a CCCV procedure during charge and a CC procedure

during discharge. The CV-step was terminated at a current of 0.5 mA.

Post-Mortem Characterization of PC_{high} (75 %)

The full cells PC_{high} (75 %) were disassembled in the discharged state after cycling for 650 cycles at 8 mA/cm². The cells were discharged to 2.7 V with a current density of 0.2 mA/cm² and then held at 2.7 V for 12 h in a CV step. The anodes and cathodes were reassembled separately in half cells with a lithium metal counter electrode in an ECC-Ref Cell (EL-Cell). Reference cells were also constructed with pristine anodes and cathodes. A glass-fiber separator (Whatman GF/C) and 400 μl of 1 mol/L LiPF_6 in EC/EMC 3:7 wt%/wt% (LP57, BASF SE) as electrolyte were used.

Current Density Test and EIS Measurements

Initially the cells were cycled five times with a current density of 0.2 mA/cm² as a formation step. This was performed in the voltage windows of 3.0–4.3 V and 0.01–1.50 V for the cathode and anode half cells, respectively. EIS measurements and a rate test of the anode and cathode lithium metal (half) cells were performed on a VMP300 galvanostat/potentiostat (BioLogic GmbH). A CV step of 3 h was applied at 3.8 V before the impedance measurements for the cathode half cells and at 0.07 V for the anode half cells to ensure that the cells are at steady-state. The impedance spectra were obtained by the perturbation of the cells with an AC voltage (amplitude: 5 mV) over the frequency range from 10 mHz to 1 MHz. The current density test was performed after the impedance measurements. The cells were cycled at 0.2, 0.5, 1.0 and 2.0 mA/cm² in the voltage windows of 3.0–4.3 V and 0.01–1.50 V for the cathode and anode half cells, respectively.

SEM Measurements

Cross-sections of the cathodes and anodes were investigated with a SEM (ZEISS Supra 25, Carl Zeiss Microscopy GmbH) using an acceleration voltage of 2 kV and a InLens detector. The cross-section preparation was conducted by cutting the cathodes with a scalpel. The pristine electrodes were uncycled anodes and cathodes, which had no contact with electrolyte. For the aged electrodes, anodes and cathodes after cycling PC_{high} (75 %) cells for 650 cycles were used (anode_{aged} (PC_{high} , 75 %, 650 cycles) and cathode_{aged} (PC_{high} , 75 %, 650 cycles)).

Acknowledgements

The authors would like to express their sincere gratitude to Marco Nimbler for preparing some of the PC electrodes and Mara Göttlinger for proof reading. The European Union's Horizon 2020 Research & Innovation program is thanked for funding the SOLIDIFY project (Grant Agreement No. 770142). Open Access funding enabled and organized by Projekt DEAL.

Conflict of Interests

The authors declare no conflict of interest.

Data Availability Statement

The data that support the findings of this study are available from the corresponding author upon reasonable request.

Keywords: Lithium-ion battery • High-loading electrodes • Aqueous processing • 3D electrode architecture • PFAS-free • Scalable production • Roll-to-roll processability

- [1] J. B. Goodenough, K.-S. Park, *J. Am. Chem. Soc.* **2013**, *135*, 1167.
- [2] J. Janek, W. G. Zeier, *Nat. Energy* **2016**, *1*, 1167.
- [3] J. Li, T. Ouyang, L. Liu, S. Jiang, Y. Huang, M.-S. Balogun, *J. Energy Chem.* **2024**, *93*, 368.
- [4] S.-H. Park, P. J. King, R. Tian, C. S. Boland, J. Coelho, C. Zhang, P. McBean, N. McEvoy, M. P. Kremer, D. Daly, J. N. Coleman, V. Nicolosi, *Nat. Energy* **2019**, *4*, 560.
- [5] D.-Y. Han, H. B. Son, S. H. Han, C. K. Song, J. Jung, S. Lee, S. S. Choi, W.-J. Song, S. Park, *Small* **2023**, *19*, e2305416.
- [6] K. G. Gallagher, S. E. Trask, C. Bauer, T. Woehrle, S. F. Lux, M. Tschech, P. Lamp, B. J. Polzin, S. Ha, B. Long, Q. Wu, W. Lu, D. W. Dees, A. N. Jansen, *J. Electrochem. Soc.* **2016**, *163*, A138–A149.
- [7] L. Wang, Y. Sun, S. Zeng, C. Cui, H. Li, S. Xu, H. Wang, *CrystEngComm* **2016**, *18*, 8072.
- [8] L. Neidhart, K. Fröhlich, F. Winter, M. Jahn, *Batteries* **2023**, *9*, 171.
- [9] J. Kim, K. Park, M. Kim, H. Lee, J. Choi, H. B. Park, H. Kim, J. Jang, Y. H. Kim, T. Song, U. Paik, *Adv. Energy Mater.* **2024**, *380*, 1324.
- [10] K. Kwon, J. Kim, S. Han, J. Lee, H. Lee, J. Kwon, J. Lee, J. Seo, P. J. Kim, T. Song, J. Choi, *Small Sci.* **2024**, *14*, 844.
- [11] H. Abe, M. Kubota, M. Nemoto, Y. Masuda, Y. Tanaka, H. Munakata, K. Kanamura, *J. Power Sources* **2016**, *334*, 78.
- [12] Z. Khanam, L. Luo, M. Mushtaq, J. Li, H. Yang, T. Ouyang, M.-S. Balogun, A. Pan, *Nano Energy* **2024**, *125*, 109590.
- [13] L. Luo, K. Liang, Z. Khanam, X. Yao, M. Mushtaq, T. Ouyang, M.-S. Balogun, Y. Tong, *Small* **2024**, *20*, e2307103.
- [14] D. L. Wood, J. Li, C. Daniel, *J. Power Sources* **2015**, *275*, 234.
- [15] H. Zheng, J. Li, X. Song, G. Liu, V. S. Battaglia, *Electrochim. Acta* **2012**, *71*, 258.
- [16] Y. Kuang, C. Chen, D. Kirsch, L. Hu, *Adv. Energy Mater.* **2019**, *9*, 1901457.
- [17] D. Parikh, T. Christensen, J. Li, *J. Power Sources* **2020**, *474*, 228601.
- [18] X. Zhang, Z. Ju, Y. Zhu, K. J. Takeuchi, E. S. Takeuchi, A. C. Marschilok, G. Yu, *Adv. Energy Mater.* **2021**, *11*, 2000808.
- [19] L. S. Kremer, A. Hoffmann, T. Danner, S. Hein, B. Prifling, D. Westhoff, C. Dreer, A. Latz, V. Schmidt, M. Wohlfahrt-Mehrens, *Energy Technol.* **2020**, *8*, 1900167.
- [20] L. Hu, F. La Mantia, H. Wu, X. Xie, J. McDonough, M. Pasta, Y. Cui, *Adv. Energy Mater.* **2011**, *1*, 1012.
- [21] P. Zhu, D. Gastol, J. Marshall, R. Sommerville, V. Goodship, E. Kendrick, *J. Power Sources* **2021**, *485*, 229321.
- [22] S. Jin, Y. Jiang, H. Ji, Y. Yu, *Adv. Mater.* **2018**, *30*, e1802014.
- [23] G. F. Yang, K. Y. Song, S. K. Joo, *J. Mater. Chem. A* **2014**, *2*, 19648.
- [24] M. Fritsch, G. Standke, C. Heubner, U. Langlotz, A. Michaelis, *J. Energy Storage* **2018**, *16*, 125.
- [25] J. Wang, M. Wang, N. Ren, J. Dong, Y. Li, C. Chen, *Energy Storage Mater.* **2021**, *39*, 287.
- [26] C. Chen, Y. Zhang, Y. Li, Y. Kuang, J. Song, W. Luo, Y. Wang, Y. Yao, G. Pastel, J. Xie, L. Hu, *Adv. Energy Mater.* **2017**, *7*, 1700595.
- [27] T. Wu, Z. Zhao, J. Zhang, C. Zhang, Y. Guo, Y. Cao, S. Pan, Y. Liu, P. Liu, Y. Ge, W. Liu, L. Dong, H. Lu, *Energy Storage Mater.* **2021**, *36*, 265.
- [28] Z. Zhao, M. Sun, W. Chen, Y. Liu, L. Zhang, N. Dongfang, Y. Ruan, J. Zhang, P. Wang, L. Dong, Y. Xia, H. Lu, *Adv. Funct. Mater.* **2019**, *29*, 1809196.
- [29] Y. Kuang, C. Chen, G. Pastel, Y. Li, J. Song, R. Mi, W. Kong, B. Liu, Y. Jiang, K. Yang, L. Hu, *Adv. Energy Mater.* **2018**, *8*, 1802398.
- [30] A. Benítez, Á. Caballero, E. Rodríguez-Castellón, J. Morales, J. Hassoun, *ChemistrySelect* **2018**, *3*, 10371.
- [31] A. Benítez, F. Luna-Lama, A. Caballero, E. Rodríguez-Castellón, J. Morales, *J. Energy Chem.* **2021**, *62*, 295.
- [32] H. Sun, J. Zhu, D. Baumann, L. Peng, Y. Xu, I. Shakir, Y. Huang, X. Duan, *Nat. Rev. Mater.* **2019**, *4*, 45.
- [33] F. Nagler, A. Flegler, G. A. Giffin, *Batter. Supercaps* **2023**, *11*, A170.
- [34] D. W. Kim, W. Y. Jo, C. W. Park, S. M. Hwang, J. B. Yoo, Y.-J. Kim, *Electrochim. Acta* **2020**, *341*, 135936.
- [35] European Chemicals Agency **2023**, <https://echa.europa.eu/documents/10162/f605d4b5-7c17-7414-8823-b49b9fd43aea>.
- [36] D. L. Wood, J. D. Quass, J. Li, S. Ahmed, D. Ventola, C. Daniel, *Dry. Technol.* **2018**, *36*, 234.
- [37] A. Wolf, F. Nagler, P. Daubinger, C. Neef, K. Mandel, A. Flegler, G. A. Giffin, *Energy Environ. Sci.* **2024**, *41*, 304.
- [38] G. D. J. Harper, E. Kendrick, P. A. Anderson, W. Mrozik, P. Christensen, S. Lambert, D. Greenwood, P. K. Das, M. Ahmeid, Z. Milojevic, W. Du, D. J. L. Brett, P. R. Shearing, A. Rastegarpanah, R. Stolk, R. Sommerville, A. Zorin, J. L. Durham, A. P. Abbott, D. Thompson, N. D. Browning, B. L. Mehdi, M. Bahri, F. Schanider-Tontini, D. Nicholls, C. Stallmeister, B. Friedrich, M. Sommerfeld, L. L. Driscoll, A. Jarvis, E. C. Giles, P. R. Slater, V. Echavarri-Bravo, G. Maddalena, L. E. Horsfall, L. Gaines, Q. Dai, S. J. Jethwa, A. L. Lipson, G. A. Leeke, T. Cowell, J. G. Farthing, G. Mariani, A. Smith, Z. Iqbal, R. Golmohammadzadeh, L. Sweeney, V. Goodship, Z. Li, J. Edge, L. Lander, V. T. Nguyen, R. J. R. Elliot, O. Heidrich, M. Slattery, D. Reed, J. Ahuja, A. Cavoski, R. Lee, E. Driscoll, J. Baker, P. Littlewood, I. Styles, S. Mahanty, F. Boons, *J. Phys. Energy* **2023**, *5*, 21501.
- [39] B. Babu, P. Simon, A. Balducci, *Adv. Energy Mater.* **2020**, *10*, 15.
- [40] M. Stein, A. Mistry, P. P. Mukherjee, *J. Electrochem. Soc.* **2017**, *164*, A1616–A1627.
- [41] A. M. Haregewoin, A. S. Wotango, B.-J. Hwang, *Energy Environ. Sci.* **2016**, *9*, 1955.
- [42] J. Illig, M. Ender, T. Chrobak, J. P. Schmidt, D. Klotz, E. Ivers-Tiffée, *J. Electrochem. Soc.* **2012**, *159*, A952–A960.
- [43] M. Steinhauer, T. Diemant, C. Heim, R. Jürgen Behm, N. Wagner, K. Andreas Friedrich, *J. Appl. Electrochem.* **2017**, *47*, 249.
- [44] M. Gaberscek, J. Moskon, B. Erjavec, R. Dominko, J. Jamnik, *J. Power Sources* **2008**, *11*, A170.
- [45] M. Hofmann, F. Nagler, M. Kapuschinski, U. Guntow, G. A. Giffin, *ChemSusChem* **2020**, *13*, 5962.
- [46] M. Hofmann, F. Nagler, U. Guntow, G. Sextl, G. A. Giffin, *J. Electrochem. Soc.* **2021**, *168*, 60511.
- [47] P. Daubinger, M. Schelter, R. Petersohn, F. Nagler, S. Hartmann, M. Herrmann, G. A. Giffin, *Adv. Energy Mater.* **2022**, *12*, 2102448.
- [48] S. Feiler, P. Daubinger, L. Gold, S. Hartmann, G. A. Giffin, *Batter. Supercaps* **2023**, *6*, e202200518.
- [49] M. Göttlinger, P. Daubinger, W. Stracke, S. Hartmann, G. A. Giffin, *Electrochim. Acta* **2022**, *419*, 140354.
- [50] F. Nagler, N. Christian, P. Daubinger, A. Flegler, M. Hofmann, G. A. Giffin, *J. Power Sources Adv.* **2023**, *24*, 100131.
- [51] P. Daubinger, M. Göttlinger, S. Hartmann, G. A. Giffin, *Batter. Supercaps* **2023**, *6*, 144.
- [52] S. Feiler, L. Gold, S. Hartmann, G. A. Giffin, *Batter. Supercaps* **2024**.
- [53] F. Nagler, N. Christian, A. Gronbach, F. Stahl, P. Daubinger, A. Flegler, M. Hofmann, G. A. Giffin, *ChemElectroChem* **2024**, *11*, A170.
- [54] P. Daubinger, F. Ebert, S. Hartmann, G. A. Giffin, *J. Power Sources* **2021**, *488*, 229457.

Manuscript received: November 13, 2024

Revised manuscript received: November 25, 2024

Accepted manuscript online: November 25, 2024

Version of record online: December 10, 2024